

# **Analysis of Stress-dependent Permeability in Nonorthogonal Flow and Deformation Fields**

By

**M. Bai<sup>1</sup>, F. Meng<sup>1</sup>, D. Elsworth<sup>2</sup>, and J.-C. Roegiers<sup>1</sup>**

<sup>1</sup>Rock Mechanics Institute, The University of Oklahoma, Norman, U.S.A.

<sup>2</sup>Department of Energy and Geo-Environmental Engineering, The Pennsylvania State University, University Park, U.S.A.

## **Summary**

The stress-dependent permeability of porous-fractured media is examined where principal stresses do not coincide with the principal permeabilities. This condition is the norm, and may arise when either flow is controlled at the local level due to the presence of inclined bedding partings or oblique fractures, or as a result of the evolving loading environment. Permeability response is controlled by shear and normal stiffnesses of fractures, frictional dilation coefficients, skeletal and grain moduli, initial permeabilities and stress state. For parameters representative of intact and fractured rocks, hydrostatic loading modes are shown to have the greatest effect in the pre-failure regime. Shear dilation effects are small, primarily controlled by the selected magnitudes of shear stiffnesses and dilation coefficients. The resulting stress-permeability relationships, which cover both fractured and intact media, are examined in a numerical study of fluid flow injected across the diameter of a cylindrical core with inclined fabric, subjected to various loading configurations. This is used to produce relationships that allow one to reduce flow test data in non-standard specimen geometries, where effective stress changes are simultaneously applied. These results confirm the significant impact of inclination of the rock fabric with respect to both flow and loading geometry on the evolving permeability field.

## **1. Introduction**

The effective large-scale composite permeability, that includes the superposed effects of fractures and matrix, is a measure of the fluid transmission capacity of a porous medium. It is one of the most important factors in determining, for example, prospective well production rates, aquifer productivity, or the likely success of remedial actions in aquifer restoration. As a result, the determination of permeability has been a focal topic in the hydrogeological sciences as well as in petroleum engineering. By definition, permeability is a physical parameter that defines transmission characteristics, independent of the properties of the percolating fluid. Correspondingly, it is closely related to the distribution of both primary or sec-

ondary porosities, and may be stress sensitive. Where fluid flow is viewed in isolation, determining the form of the permeability tensor is complicated by issues related to the representative elemental volume (REV) and in defining the orientation of the principal permeabilities. Where the pressure-sensitivity of component fractures is considered, together with the likelihood that principal stresses will not, in general, coincide with the principal permeability directions, the permeability relations are controlled in a complex fashion by the stress tensor. Correspondingly, permeability, and particularly secondary permeability, must be viewed as strongly controlled by the ambient effective stress state.

Experimental evidence indicates that the permeability of fractured media is typically at least one order of magnitude larger than that of intact media (Witherspoon et al., 1980). Envisioning the flow through fractured media as flow channeled within a set of parallel-sided conduits, makes it possible to quantify fracture permeability both numerically and experimentally (Snow, 1969; Louis, 1969; Bear, 1972; Hoek and Bray, 1977; Hsieh and Neuman, 1985; Lee et al., 1996). The anisotropic transmissive behavior of fractured media, for flow alone has been investigated by statistical methods (Sagar and Runchal, 1982; Oda, 1985), discrete modeling (Long and Witherspoon, 1985), and field flow tests (Hsieh et al., 1985). Detailed characterization of individual fractures (Hakami et al., 1995; Ge, 1997), or fracture networks (Shimo and Iihoshi, 1995) has also attracted attention in order to obtain certain crucial fracture parameters. Where stress effects are also incorporated, the emphasis has been on pore-scale models representing the porous matrix, defining behavior of the whole medium through analyzing the component behavior of the capillaries (Greenkorn, 1964; Noltimier, 1971; Ioannidis et al., 1996). Exposition of the role of pressure-sensitive fractures has primarily considered coincident principal axes of permeability and stresses (Elsworth and Xiang, 1989; Bai and Elsworth, 1994).

It is well understood that compressive loading of fractured media leads to the reduction of permeability as a result of fracture closure. Conversely, fracture opening under extensional loading results in permeability enhancement. To quantify the correlation between stress and permeability, significant experimental efforts have been made to define the relationships between the fracture aperture, subject to mechanical loading, and the initial fracture aperture. The results indicate that fracture roughness exerts a critical control (Louis, 1969; Witherspoon et al., 1980; Barton et al., 1985; Lamas, 1995). Empirical relations (Cook, 1988) show that permeability decays exponentially with the increase of normal stress. When conditions permit, laboratory testing may be used to determine the stress-permeability relations directly (Zoback and Byerlee, 1975; Rutqvist, 1995; Takahashi et al., 1995; Suri et al., 1997), and apply these to define behavior at a larger scale. At the field-scale, the stress-permeability relationships may be related to reservoir compaction (Rhett and Teufel, 1992), or soil and rock consolidation (Al-Tabbaa and Wood, 1991; Nagaraj et al., 1996), in addition to well injection or pumping (Li, 1985). Biot's (1941) theory of poroelasticity provides a comprehensive framework for the evaluation of time-dependent effective-stress fields in homogeneous media, including the incorporation of poroelastoplasticity (Morita et al., 1981; Oda, 1986). For the modeling of discretely fractured systems, explicit

stress-permeability relationships have been developed by Elsworth (1989) and Bai and Elsworth (1994) for fractured media, by Gangi (1978) and Bai and Elsworth (1994) for intact media, and by Bai et al. (1997) for fractured-porous media.

In the analysis of stress-dependent permeability, the majority of current models assume that the principal permeabilities are coincident with the principal stresses. However, such a simplification may be invalid when either the discontinuity planes are inclined with respect to the local stresses, which is likely the norm where rotations result from tectonic or human intervention. Under stress rotation, the influence of shear stresses on permeability changes may have a significant effect on the resulting permeability field. In addition, this view of non-coincident principal stress and permeability directions provides a more general definition of material anisotropies.

## 2. Stress-dependent Permeability for Fractured Media

Incorporating the influences of both normal deformation and shear dilation on the effect of fluid flow in orthogonally fractured media, the dimensionless permeability changes caused by the solid deformation may be expressed as (Elsworth and Xiang, 1989; Bai and Elsworth, 1994):

$$\frac{k}{k_0} = \left[ 1 + \frac{\Delta\varepsilon}{b} \left( \frac{K_n}{E} + \frac{1}{s} \right)^{-1} + \frac{\Delta\gamma}{b} \left( \frac{K_{sh}}{G} + \frac{1}{s} \right)^{-1} (\tan \phi_d) \right]^3, \quad (1)$$

where  $k_0$  is the initial permeability,  $\Delta\varepsilon$  and  $\Delta\gamma$  are the normal and shear strains,  $E$  and  $G$  are the elastic and shear moduli,  $b$  is the fracture aperture,  $s$  is the fracture spacing, and  $\phi_d$  is the fracture dilatational angle. This follows directly from consideration of the partitioning of strains within a fractured medium, where shear and normal stiffnesses,  $K_{sh}$  and  $K_n$ , represent the stress-deformation response of the individual fractures. This is equivalent to behavior defined in terms of a modulus reduction ratio,  $R_m = E_{mass}/E_{intact}$  (Ouyang and Elsworth, 1993; subscripts *mass* and *intact* represent the quantities in terms of rock mass or intact rock, respectively), such that,

$$\frac{k}{k_0} = \left[ 1 + \Delta\varepsilon \left( \frac{s}{b} (1 - R_m^n) + 1 \right) + \Delta\gamma \left( \frac{s}{b} (1 - R_m^s) + 1 \right) (\tan \phi_d) \right]^3, \quad (2)$$

where  $R_m^n = 1 / \left( 1 + \frac{E}{K_n s} \right)$  and  $R_m^s = 1 / \left( 1 + \frac{G}{K_{sh} s} \right)$ .

Where the standard repetitive length of individual matrix blocks, including one fracture, is taken as  $s$ , instead of  $s + b$  (since  $s \gg b$ ), then Eq. (2) collapses to Eq. (1). The integer bracketed term of Eq. (2) drops out, under this requirement. A schematic description of a three-dimensional fracture, set in a local coordinate system ( $Ox'y'z'$ ) and subjected to external load, is given in Fig. 1.

The orientations of the fracture sets can be determined from a relation between

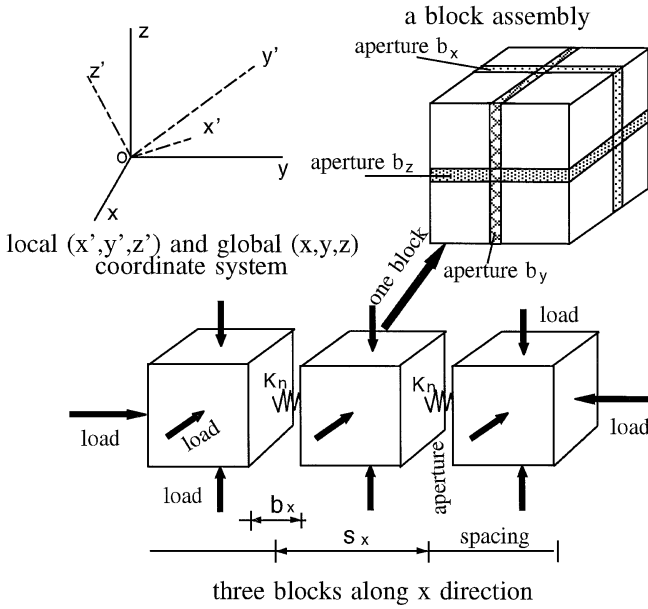


**Fig. 1.** A schematic figure showing the 3-D block-fracture geometry of the model. Matrix blocks are linked by fractures of normal stiffness,  $k_n$ , and shear stiffness,  $k_{sh}$

the global coordinate (XYZ) and the direction cosines of the fracture vector normal, i.e.,  $(l_1, m_1, n_1)$ ,  $(l_2, m_2, n_2)$ , and  $(l_3, m_3, n_3)$ . As a result, the relationship in Eq. (1) can be written more generally as follows:

$$\begin{aligned}
 \frac{k_i}{k_{0i}} = & \frac{1}{(b_j)^3 + (b_k)^3} \left\{ b_j^3 \left[ 1 + \frac{\Delta\sigma_j}{(K_n)_j b_j} + \frac{s_j - b_j}{E_j b_j} (\Delta\sigma_j - \nu_j (\Delta\sigma_i + \Delta\sigma_k)) \right. \right. \\
 & + (\Delta\tau_{jk} + \Delta\tau_{ji}) \left( \frac{G_j}{s_j} + (K_{sh})_j \right)^{-1} \frac{\tan(\phi_d)_j}{b_j} \left. \right]^3 \\
 & + b_k^3 \left[ 1 + \frac{\Delta\sigma_k}{(K_n)_k b_k} + \frac{s_k - b_k}{E_k b_k} (\Delta\sigma_k - \nu_k (\Delta\sigma_i + \Delta\sigma_j)) \right. \\
 & \left. \left. + (\Delta\tau_{kj} + \Delta\tau_{ki}) \left( \frac{G_j}{s_k} + (K_{sh})_k \right)^{-1} \frac{\tan(\phi_d)_k}{b_k} \right]^3 \right\}, \quad (3)
 \end{aligned}$$

where the subscripts  $i, j, k = x', y', z'$ ;  $i \neq j \neq k$ ;  $\nu$  is Poisson ratio, and  $\Delta\sigma$  and  $\Delta\tau$  are the normal and shear stresses.

As a specific example, the dimensionless permeability change in  $z'$  direction may be defined as:

$$\begin{aligned}
\frac{k_{z'}}{k_{0z'}} = & \frac{1}{(b_{x'})^3 + (b_{y'})^3} \left\{ b_{x'}^3 \left[ 1 + \frac{\Delta\sigma_{x'}}{(K_n)_{x'} b_{x'}} + \frac{s_{x'} - b_{x'}}{E_{x'} b_{x'}} (\Delta\sigma_{x'} - \nu_{x'} (\Delta\sigma_{y'} + \Delta\sigma_{z'})) \right. \right. \\
& + (\Delta\tau_{x'y'} + \Delta\tau_{x'z'}) \left( \frac{G_{x'}}{s_{x'}} + (K_{sh})_{x'} \right)^{-1} \frac{\tan(\phi_d)_{x'}}{b_{x'}} \left. \right]^3 \\
& + b_{y'}^3 \left[ 1 + \frac{\Delta\sigma_{y'}}{(K_n)_{y'} b_{y'}} + \frac{s_{y'} - b_{y'}}{E_{y'} b_{y'}} (\Delta\sigma_{y'} - \nu_{y'} (\Delta\sigma_{x'} + \Delta\sigma_{z'})) \right. \\
& \left. \left. + (\Delta\tau_{y'x'} + \Delta\tau_{y'z'}) \left( \frac{G_{y'}}{s_{y'}} + (K_{sh})_{y'} \right)^{-1} \frac{\tan(\phi_d)_{y'}}{b_{y'}} \right]^3 \right\}. \quad (4)
\end{aligned}$$

It should be noted that the opening or closure of the fracture, when it is subject to tension or compression, is attributed to the normal stresses only. Dilation due to shear displacements always tends to increase the fracture aperture, and correspondingly increases, the permeability magnitude (Meng and Bai, 1997), whereas the formation of gouge or post-peak strength contractile displacements will decrease permeability. Naturally, depending upon the starting point of the stress-strain relations, the shear-associated contraction may occur initially or at the stage of rock failure. However, shear induced dilation is the focus of the present study.

Transformation between local stresses and permeabilities and their global counterparts may be achieved by using the tensorial transformation properties (e.g., Jaeger and Cook, 1979). For example, the following relations can be derived for the case in which the global coordinate system ( $xyz$ ) is coincident with the principal stresses:

$$\Delta\sigma_{x'} = l_1^2 \Delta\sigma_1 + m_1^2 \Delta\sigma_2 + n_1^2 \Delta\sigma_3, \quad (5)$$

$$\Delta\sigma_{y'} = l_2^2 \Delta\sigma_1 + m_2^2 \Delta\sigma_2 + n_2^2 \Delta\sigma_3, \quad (6)$$

$$\Delta\sigma_{z'} = l_3^2 \Delta\sigma_1 + m_3^2 \Delta\sigma_2 + n_3^2 \Delta\sigma_3, \quad (7)$$

$$\Delta\tau_{x'y'} = l_1 l_2 \Delta\sigma_1 + m_1 m_2 \Delta\sigma_2 + n_1 n_2 \Delta\sigma_3, \quad (8)$$

$$\Delta\tau_{x'z'} = l_3 l_1 \Delta\sigma_1 + m_3 m_1 \Delta\sigma_2 + n_3 n_1 \Delta\sigma_3, \quad (9)$$

$$\Delta\tau_{y'z'} = l_2 l_3 \Delta\sigma_1 + m_2 m_3 \Delta\sigma_2 + n_2 n_3 \Delta\sigma_3. \quad (10)$$

Conversion of the permeabilities between the local and global systems may follow a similar process.

### 3. Stress-dependent Permeability for Intact Media

The stress-permeability relationship for intact media can be derived using the concept of Hertzian elastic contact (Timoshenko, 1934). Assuming that the change in grain size of a porous medium with a cubical packing may be related to

the external load, this relationship can be expressed as (Bai and Elsworth, 1994):

$$\frac{k}{k_0} = \left\{ 1 \mp \frac{1}{2} \left[ \frac{9(1-\nu^2)^2}{2} \left( \frac{\pi \Delta \sigma}{E} \right)^2 \right]^{1/3} \right\}^2, \quad (11)$$

where, before the second term on the right-hand side of the equation, the alternate negative and positive signs refer to compressional and dilatational loadings, respectively.

A more general formulation of the permeability changes along the  $i$  ( $i = 1, 2, 3$ ) direction, due to the changes in strains  $\Delta \varepsilon_j$  ( $j = 1, 2, 3$ ), may be expressed as:

$$\frac{k_i}{k_0} = \left[ \sum_{j=1, j \neq i}^3 \left\{ 1 - \frac{1}{2} \left[ \frac{9(1-\nu^2)^2}{2} (\pi \Delta \varepsilon_j)^2 \right]^{1/3} \right\}^2 \right], \quad (12)$$

where strains  $\Delta \varepsilon_j$  are linked to stresses  $\Delta \sigma_j$  via Hooke's strain-stress relationship, such as:

$$\begin{cases} \Delta \varepsilon_1 = \frac{1}{E} (\Delta \sigma_1 - \nu (\Delta \sigma_2 + \Delta \sigma_3)) \\ \Delta \varepsilon_2 = \frac{1}{E} (\Delta \sigma_2 - \nu (\Delta \sigma_1 + \Delta \sigma_3)) \\ \Delta \varepsilon_3 = \frac{1}{E} (\Delta \sigma_3 - \nu (\Delta \sigma_1 + \Delta \sigma_2)), \end{cases} \quad (13)$$

where the subscripts (1, 2, 3) correspond to ( $x'$ ,  $y'$ ,  $z'$ ) for a nonorthogonal flow-deformation system, and to ( $x$ ,  $y$ ,  $z$ ) for an orthogonal flow-deformation system.

Unlike in fractured media, where shear sliding between the fracture surfaces may be manifest, the effects of shear stresses within the intact porous media appear to be negligible. It is known that the application of normal stresses changes the material volume and consequently affects permeability. In contrast, no net volume change accompanies shear deformation in an elastic medium. As a result, it is assumed that permeability changes in intact media, in the pre-yield regime, are affected only by normal stresses.

#### 4. Comparative Analysis

The stress-permeability relationships presented in the previous section are further examined with a simple two-dimensional geometry in which the angle between the directions of the principal permeabilities and principal stresses is defined as  $\theta$ , as shown in Fig. 2. For simplicity, the principal stresses are assumed to be parallel to the global coordinate axes. The local stresses are related to the global stresses through the following expressions:

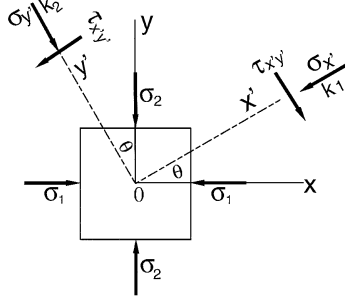


**Fig. 2.** Coordinate transformations between principal stress and permeability orientations. Principal stresses aligned with the global axes,  $(x, y)$ , are inclined at an angle  $\theta$  to the principal axes of anisotropy,  $(x', y')$

**Table 1.** Selected modeling parameters used for a two dimensional flow system

Parameter	Definition	Unit	Value
$E$	Young's modulus	MPa	$5 \times 10^3$
$K_{sh}$	fracture shear stiffness	MPa/m	$5 \times 10^2$
$K_n$	fracture stiffness	MPa/m	$5 \times 10^3$
$\nu$	Poisson ratio	–	0.2
$s_x, s_y$	fracture spacing	m	0.1
$b_x, b_y$	fracture aperture	m	0.001
$\phi_d$	fracture dilatancy angle	degree	5.37
$\theta$	inclination angle	degree	0–90

$$\Delta\sigma_{x'} = \frac{\Delta\sigma_1 + \Delta\sigma_2}{2} + \frac{\Delta\sigma_1 - \Delta\sigma_2}{2} \cos 2\theta, \quad (14)$$

$$\Delta\sigma_{y'} = \frac{\Delta\sigma_1 + \Delta\sigma_2}{2} - \frac{\Delta\sigma_1 - \Delta\sigma_2}{2} \cos 2\theta, \quad (15)$$

$$\Delta\tau_{x'y'} = \frac{\Delta\sigma_1 - \Delta\sigma_2}{2} \sin 2\theta. \quad (16)$$

With the omission of all local subscripts, the selected modeling parameters are listed in Table 1. The shear modulus can be evaluated through the relation  $G = E/2(1 + \nu)$ . For the present case, the selection of Young's modulus and Poisson ratio is representative of low permeability rocks, such as marble or granite (Jumikis, 1983). The value for the fracture normal stiffness is obtained from Bai and Elsworth (1994), in the lower part of the range reported. Finally, the fracture dilatancy angle is obtained from Elsworth and Xiang (1989), and a reasonable initial aperture of the order of 1000  $\mu\text{m}$  is selected. These values are summarized in Table 1.

Applying the stress-permeability relationship for the fractured medium [i.e., Eq. (3)], Fig. 3 shows the dimensionless permeability along the  $x'$  and  $y'$  directions with reference to the angle of inclination of the fabric,  $\theta$ . Different stress ratios

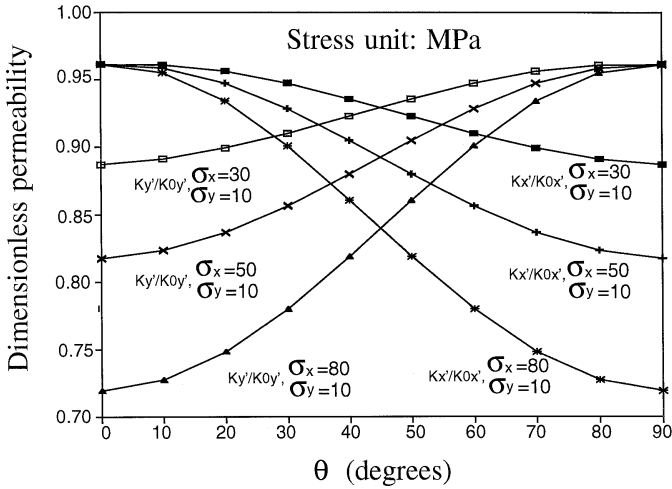


**Fig. 3.** Variation in dimensionless permeability for flow within a two-dimensional fractured medium with rotation of the principal stresses relative to the principal directions of anisotropy,  $\theta$ . High differential stress ( $\sigma_x/\sigma_y$ ); materials parameters from Table 1. Dimensionless permeability defined as the ratio of stress-modified permeability to unstressed permeability,  $k/k_0$ , as detailed in Eq. (3)

between a variable magnitude of maximum principal stress,  $\sigma_x$ , and a fixed magnitude of the minimum principal stress,  $\sigma_y$ , are used. As the normal to the fracture rotates to coincidence with the major principal stress, the permeability is a minimum. Larger principal stress magnitudes induce a greater reduction in permeability. As the normal to the fracture rotates perpendicular to the major principal stress, the permeability becomes a maximum; the permeability of the other plane, also aligned parallel to the major principal stress, also becomes a maximum. Similar behavior results for intact media, using the relationship given in Eq. (12), as shown in Fig. 4. Two noticeable differences are apparent between the responses of fractured and intact media, as identified in Figs. 3 and 4. The first is the slight difference between initial and ending values of permeability at  $\theta = 0$  and 90 degrees. The second difference is that the maximum and minimum permeabilities of the intact media no longer coincide with the orientations of the principal stresses (indicated by  $\theta$ ). These differences are explained as follows:

Examining the dimensionless permeability change in the  $x'$  direction,  $k_{x'}/k_{0x'}$ , for the present two-dimensional case, Eq. (12) can be rewritten as:

$$\begin{aligned} \frac{k_{x'}}{k_{0x'}} &= \left\{ 1 - \frac{1}{2} \left[ \frac{9(1-\nu^2)^2}{2} (\pi \Delta \varepsilon_{y'})^2 \right]^{1/3} \right\}^2 \\ &= \left\{ 1 - \frac{1}{2} \left[ \frac{9(1-\nu^2)^2}{2} \left( \frac{\pi}{E} (\Delta \sigma_{y'} - \nu \Delta \sigma_{x'}) \right)^2 \right]^{1/3} \right\}^2, \end{aligned} \quad (17)$$

where

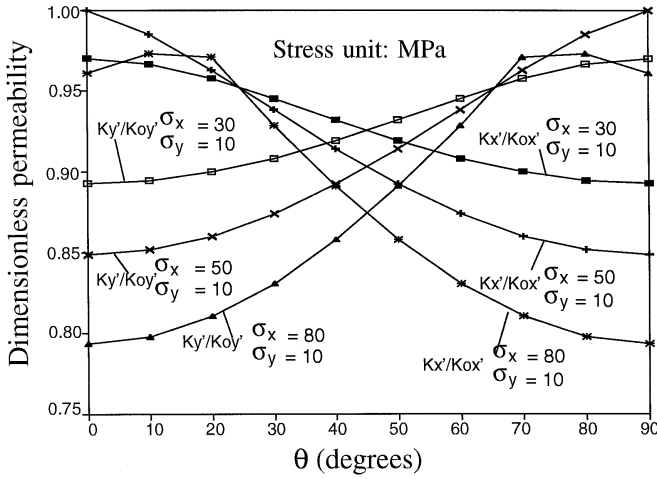


**Fig. 4.** Variation in dimensionless permeability for two-dimensional flow within an intact medium with rotation of the principal stresses relative to the principal directions of anisotropy,  $\theta$ . High differential stress ( $\sigma_x/\sigma_y$ ); material parameters from Table 1. Dimensionless permeability defined as the ratio of stress-modified permeability to unstressed permeability,  $k/k_0$ , as detailed in Eq. (12)

$$\Delta\sigma_{x'} = \frac{\Delta\sigma_x + \Delta\sigma_y}{2} + \frac{\Delta\sigma_x - \Delta\sigma_y}{2} \cos 2\theta, \quad (18)$$

$$\Delta\sigma_{y'} = \frac{\Delta\sigma_x + \Delta\sigma_y}{2} - \frac{\Delta\sigma_x - \Delta\sigma_y}{2} \cos 2\theta. \quad (19)$$

Incorporating Eqs. (18) and (19) into (17), variations of local stresses in Eq. (17) can be further defined as:

$$\Delta\varepsilon_{y'} = \frac{1}{2E} [(1 - \nu)(\Delta\sigma_x + \Delta\sigma_y) - (1 + \nu) \cos 2\theta(\Delta\sigma_x - \Delta\sigma_y)]. \quad (20)$$

It should be noted that  $\cos 2\theta$  in Eq. (20) remains positive if  $\theta$  is equal to or less than 45 degrees. For the present case (e.g.,  $\Delta\sigma_x = 80$  MPa and  $\Delta\sigma_y = 10$  MPa), the last term on the right-hand side of Eq. (20) remains negative when  $\theta$  falls between 0 and 30 degrees, which results in larger values of permeability ratio,  $k_{x'}/k_{0x'}$ , determined from Eq. (17), particularly when the stress difference is the largest.

This behavior does not occur for fractured media, where from Eq. (3), permeability changes are mainly controlled by changes in the normal stiffness of the fracture (second term on the right-hand side of the equation). A detailed discussion identifying the primary and secondary influences on permeability change [Eq. (3)] is given in a subsequent section on *Finite Element Analysis*.

Despite these differences, the resulting permeability profiles for both types of media imply the dominance of permeability variations due to the normal stress changes, since dilative changes of intact media are not incorporated into the model. Results are reported for a lower stress ratio between a fixed maximum principal stress ( $\sigma_x$ ) and a varying minimum principal stress ( $\sigma_y$ ), in Figs. 5 and 6, for fractures and intact media, respectively. Markedly different profiles of the

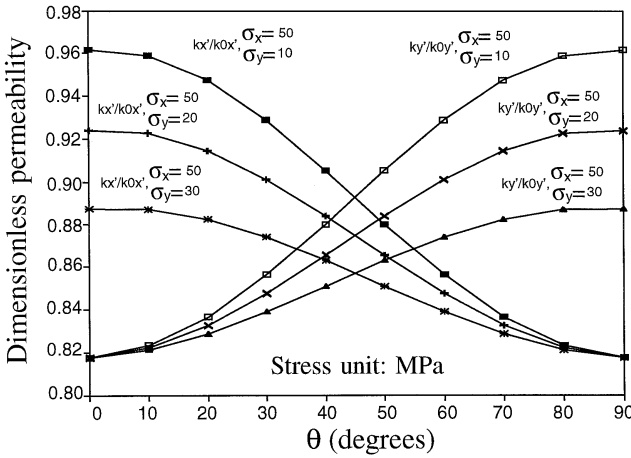


**Fig. 5.** Variation in dimensionless permeability for flow within a two-dimensional fractured medium with rotation of the principal stresses relative to the principal directions of anisotropy,  $\theta$ . Moderate differential stress ( $\sigma_x/\sigma_y$ ); material parameters from Table 1. Dimensionless permeability defined as the ratio of stress-modified permeability to unstressed permeability,  $k/k_0$ , as detailed in Eq. (3)

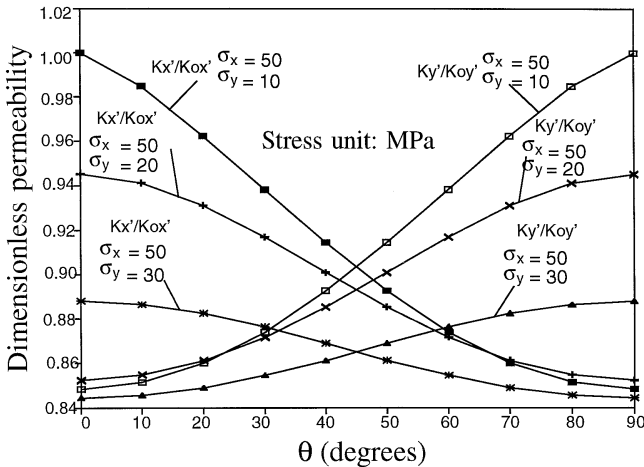


**Fig. 6.** Variation in dimensionless permeability for two-dimensional flow within an intact medium with rotation of the principal stresses relative to the principal directions of anisotropy,  $\theta$ . Moderate differential stress ( $\sigma_x/\sigma_y$ ); material parameters from Table 1. Dimensionless permeability defined as the ratio of stress-modified permeability to unstressed permeability,  $k/k_0$ , as detailed in Eq. (12)

permeability changes, relative to the previous cases for fractured and intact media, result. The permeability response increases monotonically with the inclination of the fabric to the principal stresses, for this moderate level of the stress ratios. The resulting changes in permeability with rotation of the stress tensor for low stress ratios are shown in Figs. 7 and 8. The comparative analysis reveals the strong influence of the stress state.

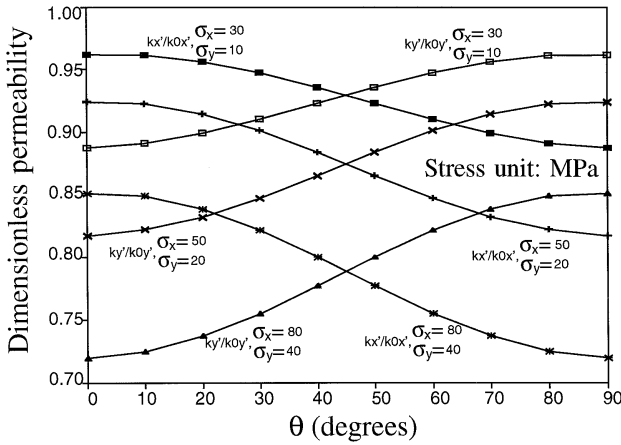


Fig. 7. Variation in dimensionless permeability for flow within a two-dimensional fractured medium with rotation of the principal stresses relative to the principal directions of anisotropy,  $\theta$ . Low differential stress ( $\sigma_x/\sigma_y$ ); material parameters from Table 1. Dimensionless permeability defined as the ratio of stress-modified permeability to unstressed permeability,  $k/k_0$ , as detailed in Eq. (3)

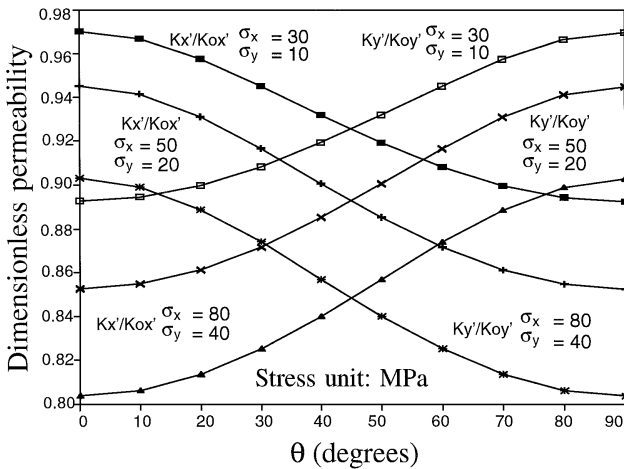
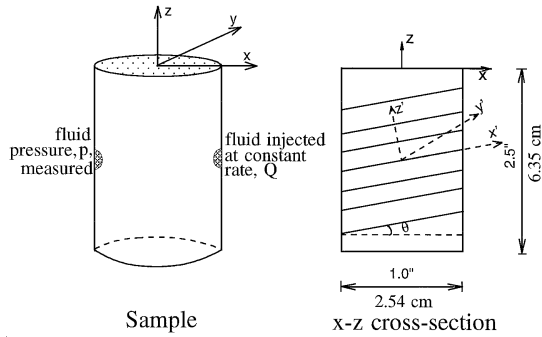


Fig. 8. Variation in dimensionless permeability for two-dimensional flow within an intact medium with rotation of the principal stresses relative to the principal directions of anisotropy,  $\theta$ . Low differential stress ( $\sigma_x/\sigma_y$ ); material parameters from Table 1. Dimensionless permeability defined as the ratio of stress-modified permeability to unstressed permeability,  $k/k_0$ , as detailed in Eq. (12)

### 5. Parametric Analyses

Conducting laboratory fluid flow tests in cored rock specimens is a useful means to determine the anisotropic characteristics and permeabilities of aquifers and reservoir rocks. However, in addition to the expense involved, most laboratory tests are difficult to perform due to complications in the test design, instrumental setup, flow rate control, fluid leakage management, and specimen preparation. Conse-



**Fig. 9.** Geometry of the cylindrical specimen used in flow tests. Principal stresses are aligned along the  $(x, y, z)$  coordinate system, with the fracture system defined relative to  $(x', y', z')$

quently, the effort of modeling to represent true test conditions, and to recover the maximum information from the test, appears worthwhile. Numerical analyses using the finite element technique are described in the following, with ‘test’ referring to the ‘numerical replication’ process.

### 5.1 Test Specifications

The specimen geometry, based on specific test configurations, was provided by a petroleum company. The tests are constrained for fluid to flow through cylindrical core specimens with the bedding inclined at an angle  $\theta$  between 0 to 30 degrees with the horizontal plane (i.e., the angle between bedding plane and  $x$  axis). As a result, the bedding fractures affect the fluid flow along the primary  $x$  orientation. Parallel orthogonal fractures are embedded within the specimens with their planes being coincident with the local coordinate system  $(x'/y'/z')$ . The initial specimen geometry is 2.5 inch (6.35 cm) in height and 1.0 inch (2.54 cm) in diameter. Inlet and outlet are small circular holes of 0.25 inch (0.635 cm) in diameter, placed on opposite sides of the specimen, as indicated in Fig. 9. During the tests, a constant flow rate,  $Q$ , is applied while fluid pressure,  $p$ , is measured at the outlet. The injection area is approximately  $0.04 \text{ in}^2$  ( $0.258 \text{ cm}^2$ ). The selected parameters are listed in Table 2. Young’s modulus and Poisson ratio are chosen as representative of sandstone and limestone (Jumikis, 1983). The value for the fracture normal stiffness is obtained from the relationship in Bai and Elsworth (1994). Spacing of micro-fractures within the specimen is selected as 0.1 mm, with an initial aperture an order-of-magnitude lower, as defined in Table 2, yielding a secondary porosity of approximately 10%. For the selected fracture spacing, approximately 5 micro-fractures intersect the injection area.

### 5.2 Loading Configurations

The test specimen is subjected to axial and radial principal stresses (e.g.,  $\sigma_z = \sigma_1$ ,  $\sigma_x = \sigma_2$  and  $\sigma_y = \sigma_3$ ). Five loading configurations are selected and itemized in

**Table 2.** Selected modeling parameters for fluid injection into a central horizontal hole of a cylindrical specimen

Parameter	Definition	Unit	Value
$E$	Young's modulus	MPa	$3 \times 10^4$
$K_{sh}$	fracture shear stiffness	MPa/m	$3 \times 10^5$
$K_n$	fracture stiffness	MPa/m	$3 \times 10^6$
$\nu$	Poisson ratio	–	0.2
$s_x, s_y, s_z$	fracture spacing	m	0.001
$b_x, b_y, b_z$	fracture aperture	m	0.0001
$\phi_d$	fracture dilatancy angle	degree	5
$\theta$	inclination angle	degree	0–90

**Table 3.** Selected loading configurations for cylindrical specimens subject to lateral injection

Case	Loading	$\sigma_1$	$\sigma_2$	$\sigma_3$	Value
1	no	0	0	0	MPa
2	uniaxial	100	0	0	MPa
3	triaxial	100	50	50	MPa
4	polyaxial	100	75	50	MPa
5	hydrostatic	100	100	100	MPa

Table 3, including uniaxial and triaxial conditions applicable to cylindrical laboratory specimens. An additional polyaxial load case is included, approximately representing conditions in a stressed block.

### 5.3 Stress– $\theta$ Relationship under Different Loadings

Referring to Fig. 9, the global ( $xyz$ ) and local ( $x'y'z'$ ) coordinates are correlated by the directional cosines:

$$l_1 = \cos \theta, \quad m_1 = 0, \quad n_1 = \sin \theta, \quad (21)$$

$$l_2 = 0, \quad m_2 = 1, \quad n_2 = 0, \quad (22)$$

$$l_3 = -\sin \theta, \quad m_3 = 0, \quad n_3 = \cos \theta. \quad (23)$$

If the layers are inclined only relative to the  $x$  and  $z$  coordinates, the two-dimensional stress transformation equations resulting from Eqs. (5) through (10), reduce to:

$$\Delta\sigma_{x'} = \Delta\sigma_x \cos^2 \theta + \Delta\sigma_z \sin^2 \theta, \quad (24)$$

$$\Delta\sigma_{y'} = \Delta\sigma_y, \quad (25)$$

$$\Delta\sigma_{z'} = \Delta\sigma_x \sin^2 \theta + \Delta\sigma_z \cos^2 \theta, \quad (26)$$

$$\Delta\tau_{x'y'} = \Delta\tau_{y'x'} = 0, \quad (27)$$

$$\Delta\tau_{y'z'} = \Delta\tau_{z'y'} = 0, \quad (28)$$

$$\Delta\tau_{z'x'} = \Delta\tau_{x'z'} = \cos \theta \sin \theta (\Delta\sigma_z - \Delta\sigma_x). \quad (29)$$

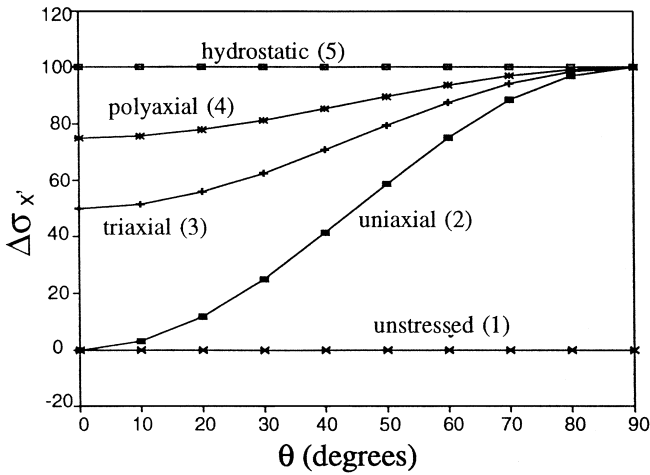


**Fig. 10.** Change in normal stress parallel to the anisotropy,  $\Delta\sigma_x$ , with variation in the inclination,  $\theta$ , of the applied principal stress, to the orientations of fractures. Loading conditions are defined in Table 3

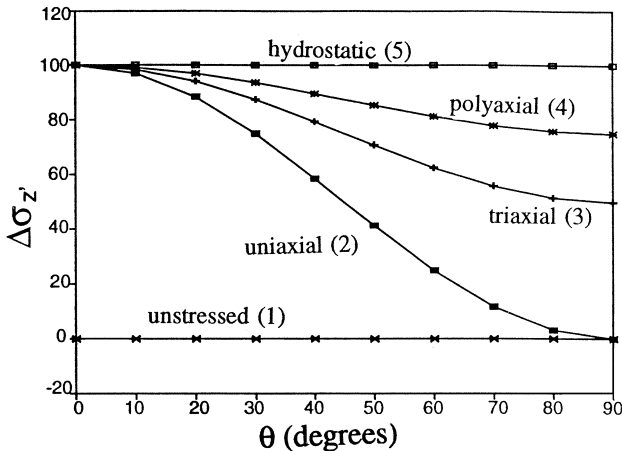


**Fig. 11.** Change in normal stress perpendicular to the anisotropy,  $\Delta\sigma_z$ , with variation in the inclination,  $\theta$ , of the applied principal stress, to the orientations of fractures. Loading conditions are defined in Table 3

Five loading configurations are analyzed, as listed in Table 3, with the relationships between the local stresses and the angle of inclination  $\theta$ , as given in Eqs. (24) through (29).

Stresses acting on fracture planes, inclined at  $\theta$  to the principal stress,  $\sigma_z$ , are illustrated in Figs. 10–13. Hydrostatic and unstressed states yield invariant stresses with the inclination of the fracture planes, while loading configurations with a deviatoric load result in variable normal and shear stresses. Out-of-plane loading

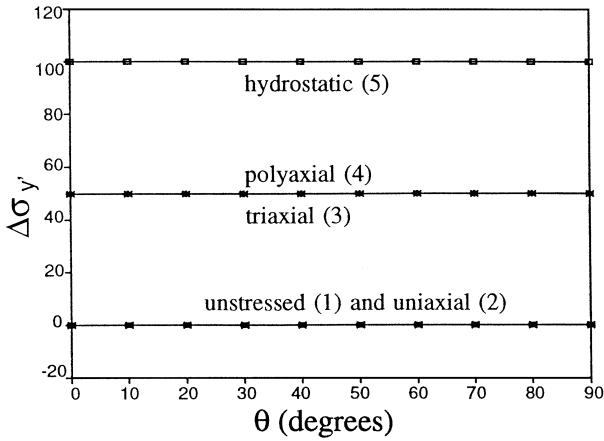


**Fig. 12.** Change in normal stress parallel to the anisotropy,  $\Delta\sigma_y$ , with variation in the inclination,  $\theta$ , of the applied principal stress, to the orientations of fractures. Loading conditions are defined in Table 3

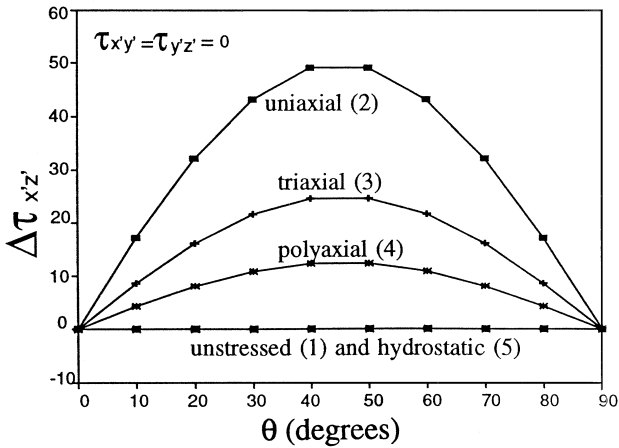


**Fig. 13.** Change in shear stress acting on the fracture planes,  $\Delta\tau_{x'z'}$ , with variation in the inclination,  $\theta$ , of the applied principal stress, to the fractures. Loading conditions are defined in Table 3

is invariant, as shown in Fig. 12, and shear stresses are a maximum on planes inclined at 45°, and zero on the principal planes as shown in Fig. 13.

#### 5.4 Permeability-Stress Equations

Incorporating the fracture aperture changes resulting from the changes in normal stresses and shear stresses, applying the simplified assumptions that all the

parameters are independent of the coordinate systems, as well as that  $b_i = b_j = b_k$ , the modified dimensionless permeabilities along local,  $x'$ ,  $y'$  and  $z'$  directions, may be defined, according to Eq. (3), as:

$$\begin{aligned} \frac{\Delta k_{x'}}{k_{0x'}} = \frac{1}{2} & \left\{ \left[ 1 - \frac{\Delta\sigma_{y'}}{K_n b} + \frac{s_{y'} - b}{Eb} (\Delta\sigma_{y'} - \nu(\Delta\sigma_{x'} + \Delta\sigma_{z'})) \right]^3 \right. \\ & + \left[ 1 - \frac{\Delta\sigma_{z'}}{K_n b} + \frac{s_{z'} - b}{Eb} (\Delta\sigma_{z'} - \nu(\Delta\sigma_{x'} + \Delta\sigma_{y'})) \right. \\ & \left. \left. + (\Delta\tau_{z'x'}) \left( \frac{G}{s_{z'}} + K_{sh} \right)^{-1} \frac{\tan \phi_d}{b} \right]^3 \right\} \end{aligned} \quad (30)$$

$$\begin{aligned} \frac{\Delta k_{y'}}{k_{0y'}} = \frac{1}{2} & \left\{ \left[ 1 - \frac{\Delta\sigma_{x'}}{K_n b} + \frac{s_{x'} - b}{Eb} (\Delta\sigma_{x'} - \nu(\Delta\sigma_{y'} + \Delta\sigma_{z'})) \right. \right. \\ & \left. \left. + (\Delta\tau_{z'x'}) \left( \frac{G}{s_{x'}} + K_{sh} \right)^{-1} \frac{\tan \phi_d}{b} \right]^3 \right. \\ & + \left[ 1 - \frac{\Delta\sigma_{z'}}{K_n b} + \frac{s_{z'} - b}{Eb} (\Delta\sigma_{z'} - \nu(\Delta\sigma_{y'} + \Delta\sigma_{x'})) \right. \\ & \left. \left. + (\Delta\tau_{z'x'}) \left( \frac{G}{s_{z'}} + K_{sh} \right)^{-1} \frac{\tan \phi_d}{b} \right]^3 \right\} \end{aligned} \quad (31)$$

$$\begin{aligned} \frac{\Delta k_{z'}}{k_{0z'}} = \frac{1}{2} & \left\{ \left[ 1 - \frac{\Delta\sigma_{x'}}{K_n b} + \frac{s_{x'} - b}{Eb} (\Delta\sigma_{x'} - \nu(\Delta\sigma_{y'} + \Delta\sigma_{z'})) \right. \right. \\ & \left. \left. + (\Delta\tau_{z'x'}) \left( \frac{G}{s_{x'}} + K_{sh} \right)^{-1} \frac{\tan \phi_d}{b} \right]^3 \right. \\ & \left. \left. + \left[ 1 - \frac{\Delta\sigma_{y'}}{K_n b} + \frac{s_{y'} - b}{Eb} (\Delta\sigma_{y'} - \nu(\Delta\sigma_{x'} + \Delta\sigma_{z'})) \right]^3 \right\}. \end{aligned} \quad (32)$$

### 5.5 Finite Element Analysis

For modeling steady state fluid flow through the cylindrical specimen, a three-dimensional finite element model is assembled, using eight-node isoparametric

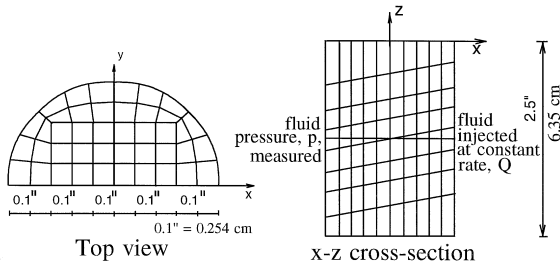


**Fig. 14.** Finite element mesh within the cylindrical specimen. Half symmetry is used. The mesh is invariant with fracture inclination,  $\theta$

**Table 4.** Permeability versus inclination of bedding to principal stress direction,  $\theta$ , for the loading configurations of Table 3 (unit: md)

Loading case	Permeability	$\theta$			
		0°	30°	60°	90°
1	$k_{x'}$	100	100	100	100
	$k_{y'}$	100	100	100	100
	$k_{z'}$	100	100	100	100
2	$k_{x'}$	86.63	89.71	96.34	99.88
	$k_{y'}$	86.63	86.17	86.17	86.63
	$k_{z'}$	99.88	96.34	89.71	86.63
3	$k_{x'}$	79.57	81.08	84.22	85.85
	$k_{y'}$	79.57	79.46	79.46	79.57
	$k_{z'}$	85.85	84.22	81.08	79.57
4	$k_{x'}$	79.54	80.29	81.82	82.60
	$k_{y'}$	76.32	76.30	76.30	76.32
	$k_{z'}$	82.59	81.82	80.29	79.54
5	$k_{x'}$	73.19	73.19	73.19	73.19
	$k_{y'}$	73.19	73.19	73.19	73.19
	$k_{z'}$	73.19	73.19	73.19	73.19

brick elements (Bai and Meng, 1994) and a protocol to accommodate the coupled nature of the flow-deformation system (Bai and Elsworth, 1994). The finite element mesh arrangement is depicted in Fig. 14, in which eight layers inclined with respect to the horizontal plane are incorporated. Each inclined plane consists of 42 elements, which results in a total of 486 nodes and 336 elements.

Assuming an isotropic rock specimen with an initial permeability of  $k_{x'} = k_{y'} = k_{z'} = 100$  md (milli darcy), applying uniform fracture spacing (i.e.,  $s_i = s_j = s_k$ ), and the other parameters listed in Table 2, enables mean permeability magnitudes to be determined, as reported in Table 4.

Figs. 15, 16 and 17 show the relative permeability magnitudes resulting from different external loadings along the  $x'$ ,  $y'$  and  $z'$  directions with respect to differ-

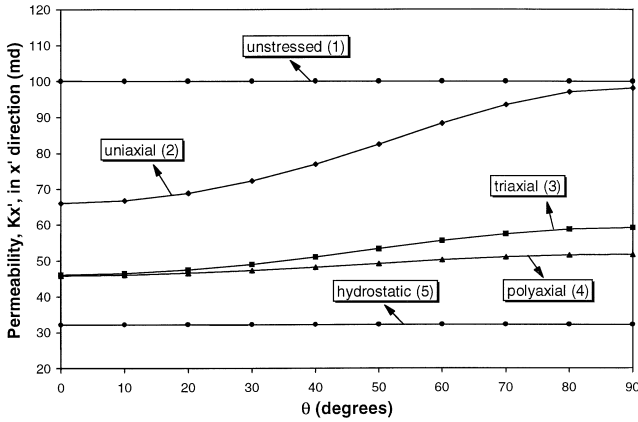


Fig. 15. Change in permeability parallel to the fracture  $k'_{x'}$ , with varying inclination  $\theta$  of the fracture system relative to the specimen axis. Load conditions are defined in Table 3

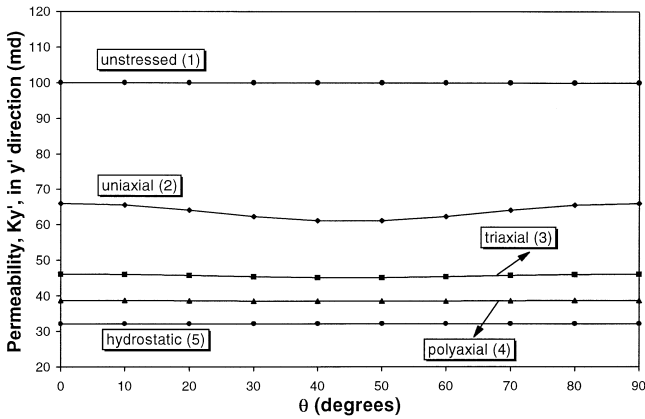


Fig. 16. Change in permeability parallel to the fracture  $k'_{y'}$ , with varying inclination  $\theta$  of the fracture system relative to the specimen axis. Load conditions are defined in Table 3

ent angles of inclination of the fracture planes,  $\theta$ . Similar to the previous two-dimensional cases, permeability changes are dominated by changes in normal stresses induced across the fracture planes, especially for uniaxial loading. The dominant influence of normal stresses on the change in permeability is the most obvious along the  $x'$  and  $z'$  directions. Hydrostatic loading yields the maximum change in permeability, relative to the unstressed permeability. As expected, triaxial and polyaxial loadings are intermediate between these limiting values. The dominant role of normal stresses may be shown by splitting the right-hand side of Eq. (30) into the following five parts (except the terms related to the value 1); i.e.,

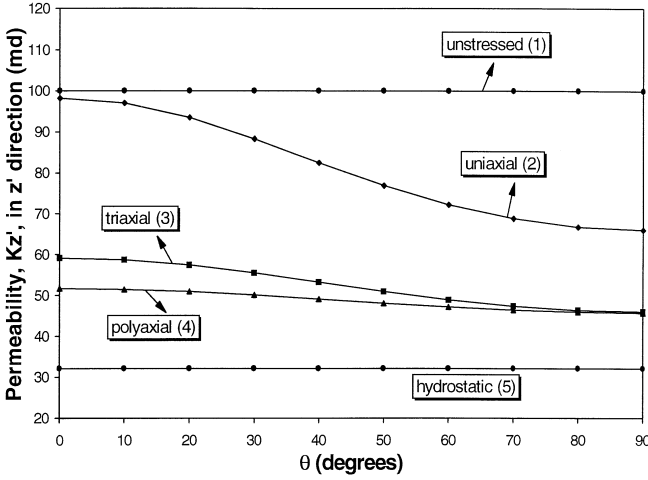


Fig. 17. Change in permeability perpendicular to the fracture  $k'_z$  with varying inclination  $\theta$  of the fracture system relative to the specimen axis. Load conditions are defined in Table 3

$$\left\{ \begin{array}{l} \text{Part 1 : } \frac{\Delta\sigma_{y'}}{K_n b}, \\ \text{Part 2 : } \frac{s_{y'} - b}{Eb} [\Delta\sigma_{y'} - \nu(\Delta\sigma_{x'} + \Delta\sigma_{z'})], \\ \text{Part 3 : } \frac{\Delta\sigma_{z'}}{K_n b}, \\ \text{Part 4 : } \frac{s_{z'} - b}{Eb} [\Delta\sigma_{z'} - \nu(\Delta\sigma_{x'} + \Delta\sigma_{y'})], \\ \text{Part 5 : } \Delta\tau_{z'x'} \left( \frac{G}{s_{z'}} + K_{sh} \right)^{-1} \frac{\tan \phi_d}{b}. \end{array} \right. \quad (33)$$

Under triaxial loading (case 3), Fig. 18 depicts the magnitudes of the permeabilities contributed by each part of Eq. (33), respectively. Unlike the contributions from the normal stresses (parts 1 to 4), it is easily seen that the change in shear stresses (part 5) plays a minor role in the associated permeability changes. This results from the low magnitude of dilation angle,  $\phi_d$ , selected in the analysis, with shear effects anticipated to be larger for lower confining stresses, lower shear stiffnesses, and increased angles of dilation.

### 5.6 Equivalent Geometric Factor

It is common practice to determine laboratory permeability magnitudes,  $k$ , by conducting steady state flow tests. Permeability is derived from the test data using

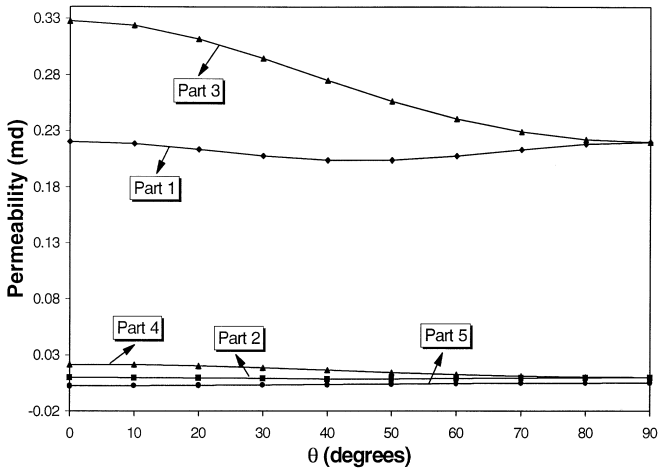


**Fig. 18.** Permeability (md) components resulting from normal (parts 1 and 3), Poisson (parts 2 and 4) and shear (part 5) components, defined in Eq. (29). Variation with relative inclination  $\theta$  of fracture fabric

a modified Darcy's law in which a 'geometric factor' is used to relate the actual flow geometry to an ideal geometry. For the flow geometry defined in Fig. 9, the cross-sectional area of flow is not constant. The flow geometry that results in this specimen geometry may be represented as a function of specimen dimensions, inlet/outlet area and angle of inclination of the flow anisotropy. The desire is to provide a geometric factor that allows permeability to be calculated directly with reference to the measurable inlet port area, alone. This obviates the need to complete numerical simulations for the reduction of all data, since the geometric correction factor may be defined from the following. This geometric factor becomes an 'equivalent' value for the tests involved in the external loading since this conversion factor incorporates not only the geometric variations between actual and analytical flow cross-sectional areas, but also the specimen spatial changes as a result of the mechanical loading. The evaluation of correction factors, incorporating both geometric and stress effects, is only possible with the aid of numerical modeling.

Darcy's law can be written in a general form as:

$$Q = -A \frac{k}{\mu} \frac{\Delta p}{L}, \quad (34)$$

where  $A$  is the uniform flow cross-sectional area and  $L$  is the flow length across the domain.

Assuming that the subscript 't' indicates the quantity from the test or numerical simulation, where the geometry of Fig. 9 is used, while the subscript 'a' implies the analytically calculated values for a constant flow cross-sectional area, Darcy's law can be written symbolically for each individual situation as:

$$q_t = -A_t \frac{k_t}{\mu} \frac{\Delta p_t}{L}, \quad (35)$$

$$q_a = -A_a \frac{k_a}{\mu} \frac{\Delta p_a}{L}; \quad (36)$$

If steady state flow conditions prevail, one has:

$$q_t = q_a, \quad k_t = k_a. \quad (37)$$

However, if the influence of the external load is incorporated, Eq. (37) should be modified as:

$$q_t^* = q_t - \Delta q_t = q_a, \quad k_t^* = k_t - \Delta k_t = k_a, \quad (38)$$

where  $\Delta q_t$  and  $\Delta k_t$  are the changes of flow rate and permeability due to the stress changes.

Let the modified Darcy's law with reference to the loading environment be given as:

$$q_t^* = -A_t \frac{k_t^*}{\mu} \frac{\Delta p_t}{L}. \quad (39)$$

Substituting Eq. (38) into (39), gives:

$$q_t^* = -A_t \frac{k_t - \Delta k_t}{\mu} \frac{\Delta p_t}{L}. \quad (40)$$

The equivalent geometric factor  $G^*$  can be obtained by equating Eq. (36) to (40), which results in (Bai and Meng, 1997):

$$G^* = \frac{\Delta p_t}{\Delta p_a} = \frac{A_a k_a}{A_t (k_t - \Delta k_t)}. \quad (41)$$

In general,  $A_a \leq A_t$ , therefore,  $G^* \leq 1$ .

The utility of the geometric factor,  $G^*$  is to relate laboratory flow rates and pressure drops, measured within a non-standard specimen geometry to invariant magnitudes of permeability,  $k_a$ . When there is no change due to mechanical effects,  $\Delta k_t = 0$  and the factor relates purely to the mismatch in geometries. In this situation  $G^*$  represents the ratio of pressure drop measured in the cross-specimen test (Fig. 9) to that measured, say longitudinally within a constant diameter core. It is a purely geometric correction for the selected test geometry where the same volumetric flow rate occurs in each test. Similarly, where mechanical changes in permeability are applied to the specimen,  $G^*$  represents the ratios of pressure drops in the actual testing configuration to that for a longitudinal test within a core. Now stress and geometric effects are included in the result, making it possible to conveniently determine the anticipated mechanical effect on reservoir permeability for any desired specimen configurations. Prior evaluation for magnitudes of  $G^*$  enables one to directly deduce permeability magnitudes from laboratory data from non-standard specimens, and to extrapolate them to define expected magnitudes of permeability change in altered stress fields.

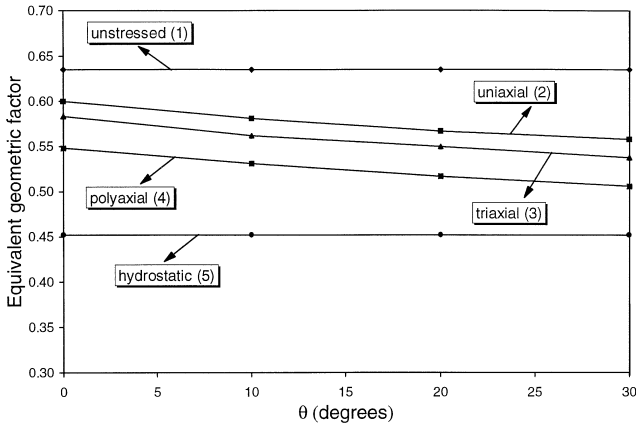


**Fig. 19.** Change in the equivalent geometric factor,  $G^*$ , of Eq. (41), with inclination angle,  $\theta$ . Loading cases are as described in Table 3

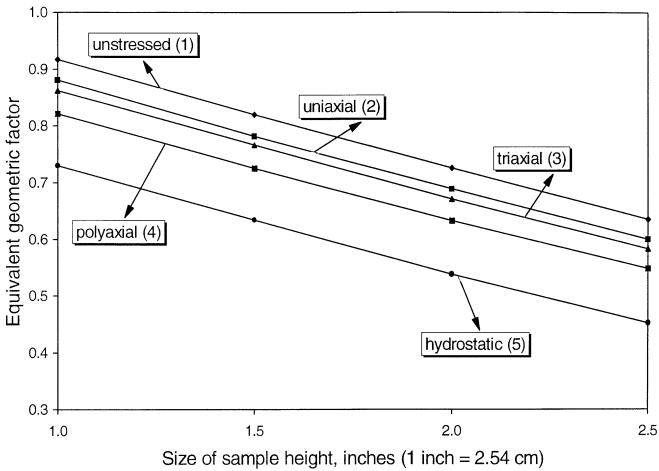


**Fig. 20.** Change in the equivalent geometric factor,  $G^*$ , of Eq. (41), with specimen height. Loading cases are as described in Table 3

The relationships between the equivalent geometric factor and the angle of inclination of micro-fractures may be derived from the numerical modeling for a variety of loading conditions, as shown in Fig. 19. Except for unstressed and hydrostatically loaded specimens, the geometric factors decrease with an increase in  $\theta$ , showing the effect of normal stresses in reducing permeability magnitudes. Larger equivalent geometric factors, in general, represent a greater effect of external loading. In view of the specimen size effect, four different specimen size combinations are selected using identical specimen diameters but different specimen heights, ranging from 1.0 inch to 2.5 inches (2.54 cm to 6.35 cm), respectively. For the case of  $\theta = 0^\circ$ , Fig. 20 depicts the relationships between the equivalent geo-

metric factors and different specimen heights for various loading conditions. The equivalent geometric factors decrease with the increase of the specimen heights for all loading cases. In general, the greater the specimen height, the smaller the external load, the smaller the equivalent geometric factor.

## 6. Conclusions

Analytical relationships between permeability and stress variation are presented where the principal permeability directions are not coincident with the principal stress directions in a general three-dimensional geometry, and for both fractured and intact media. These relationships are the most relevant for characterizing coupled flow-deformation phenomena, where: (a) inclined bedding partings are embedded in fractured porous media, (b) inlet and outlet locations induce flow that is different from the principal permeability directions of the media, and (c) principal stresses are not coincident with the principal flow orientations. These conditions are common in subsurface hydrogeological and geomechanical environments; however, they are typically ignored by the majority of models for both convenience and simplicity. The permeability changes resulting from the non-alignment of principal stresses and principal permeability directions are shown to be significant. Using a comparative example and case studies, numerical modeling highlights the important differences between: (a) two-dimensional and three-dimensional modeling (e.g., the dominant effects of normal and shear stresses); (b) the contrasting pressure sensitivities of fractured and intact media (e.g., the minimal impact of shear stresses in inducing permeability changes in porous media); (c) the impact of different loading configurations (e.g., the minimal and maximal effects of unstressed and hydrostatically stressed conditions); and (d) the importance of various angles of inclination of the fabric within these systems (e.g., maximized effect for shear at  $\theta = 45^\circ$ , etc.)

## Acknowledgements

The authors are most grateful to Dr. M. Zaman for his useful comments, suggestions which certainly improve our understanding of the problem. Thanks are also due to Dr. T. Scott of the Rock Mechanics Institute and Dr. David Yale from Mobil for their constructive comments and suggestions. Support of National Science Foundation/State/Industry under contract EEC9209619 and under the S/IUCRC program is also gratefully acknowledged.

## References

- Al-Tabbaa, A., Wood, D. M. (1991): Horizontal drainage during consolidation: insights gained from analyses of a simple problem. *Géotechnique* 41, 571–585.
- Bai, M., Elsworth, D. (1994): Modeling of subsidence and stress-dependent hydraulic conductivity for intact and fractured porous media. *Rock Mech. Rock Engng.* 27, 209–234.
- Bai, M., Meng, F. (1994): Study of naturally fractured reservoirs using three-dimensional finite elements. Internal Report RMRC-94-19, University of Oklahoma.

- Bai, M., Meng, F. (1997): Analysis of stress-dependent permeability: homogeneous anisotropic porous media. RMC-97-01, Rock Mechanics Institute, The University of Oklahoma.
- Bai, M., Meng, F., Elsworth, D., Zaman, M., Roegiers, J.-C. (1997): Numerical modeling of stress-dependent permeability. *Int. J. Rock Mech. Min. Sci.* 34, 446.
- Barton, N., Bandis, S., Bakhtar, K. (1985): Strength, deformation and conductivity coupling of rock joints. *Int. J. Rock Mech. Min. Sci. Geomech. Abstr.* 22, 121–140.
- Bear, J. (1972): *Dynamics of fluids in porous media*. Elsevier, Amsterdam, 764p.
- Biot, M. A. (1941): General theory of three dimensional consolidation. *J. Appl. Phys.* 12, 155–164.
- Cook, N. G. W. (1988): Natural joints in rock: mechanical, hydraulic and seismic behavior and properties under normal stress. 1st Jaeger Memorial Lecture, University of Minnesota.
- Elsworth, D. (1989): Thermal permeability enhancement of blocky rocks: one dimensional flows. *Int. J. Rock Mech. Min. Sci. Geomech. Abstr.* 26(3/4), 329–339.
- Elsworth, D., Xiang, J. (1989): A reduced degree of freedom model for thermal permeability enhancement in blocky rock. *Geothermics* 18, 691–709.
- Gangi, A. F. (1978): Variation of whole and fractured porous rock permeability with confining pressure. *Int. J. Rock Mech. Min. Sci. Geomech. Abstr.* 15(3), 249–257.
- Ge, S. (1997): A governing equation for fluid flow in rough fractures. *Water Resour. Res.* 33, 53–61.
- Greenkorn, R. A. (1964): Directional permeability of heterogeneous anisotropic porous media. *Soc. Petrol. Engin. J.* 16, 124–132.
- Hakami, E., Einstein, H. H., Gentier, S., Iwano, M. (1995): Characterization of fracture apertures – methods and parameters. *Proc., 8th Int. Congress on Rock Mechanics, Japan*, 751–754.
- Hoek, E., Bray, J. W. (1977): *Rock slope engineering*, 2nd edn. The Institute of Mining and Metallurgy, London, 402p.
- Hsieh, P. A., Neuman, S. P. (1985): Field determination of the three-dimensional hydraulic conductivity tensor of anisotropic media. *Water Resour. Res.* 21, 1655–1665.
- Hsieh, P. A., Neuman, S. P., Stiles, G. K., Simpson, E. S. (1985): Field determination of the three-dimensional hydraulic conductivity tensor of anisotropic media. 2. Methodology and application to fractured rocks. *Water Resour. Res.* 21, 1667–1676.
- Ioannidis, M. A., Kwiecien, M. J., Chatzis, I. (1996): Statistical analysis of the porous microstructure as a method for estimating reservoir permeability. *J. Petrol. Sci. Eng.* 16, 251–261.
- Jaeger, J. C., Cook, N. G. W. (1979): *Fundamentals of rock mechanics*, 3rd edn. Chapman and Hall, London.
- Jumikis, A. R. (1983): *Rock mechanics*, 2nd edn. Trans Tech Publications, Chansferal.
- Lamas, L. N. (1995): An experimental study of the hydromechanical properties of granite joints. *Proc., 8th Int. Congress on Rock Mechanics, Japan*, 733–738.
- Lee, C.-H., Chang, J.-L., Hsu, K.-T. (1996): Investigation of hydraulic aperture at surface-exposed rock fractures in situ. *Géotechnique* 46, 343–349.
- Li, V. C. (1985): Estimation of in-situ hydraulic diffusivity of rock masses. *PAGEOPH* 122, 545–559.

- Long, J. C. S., Witherspoon, P. A. (1985): The relationship of the degree of interconnection to permeability in fracture networks. *J. Geophys. Res.* 90, 3087–3098.
- Louis, C. (1969): Groundwater flow in rock masses and its influence on stability. *Rock Mech. Research Report 10*, Imperial College, London.
- Meng, F., Bai, M. (1997): Modeling flow in oblique fractured porous media in arbitrary stress field. Report RMRC-97-07.
- Morita, N., Gray, K. E., Kim, C. M. (1981): Stress state, porosity, permeability and breakdown pressure around a borehole during fluid injection. *Proc., 22th U.S. Symp. on Rock Mech.*, MIT, MA.
- Nagaraj, T. S., Pandian, N. S., Narasimha Raju, P. S. R. (1994): Stress-state-permeability relations for overconsolidated clays. *Géotechnique* 46, 363–366.
- Noltimier, H. C. (1971): A model for grain dispersion and magnetic anisotropy in sedimentary rocks. *J. Geophys. Res.* 76, 3990–4002.
- Oda, A. (1985): Permeability tensor for discontinuous rock masses. *Géotechnique* 35, 483–495.
- Oda, M. (1986): An equivalent continuum model for coupled stress and fluid flow analysis in jointed rock masses. *Water Resour. Res.* 22, 1845–1856.
- Ouyang, Z., Elsworth, D. (1993): Evaluation of groundwater flows into mined panels. *Int. J. Rock Mech. Min. Sci. Geomech. Abstr.* 30, 2, 71–79.
- Rhett, D. W., Teufel, L. W. (1992): Stress path dependence of matrix permeability of North Sea sandstone reservoir rock. *Proc., 33th U.S. Symp. on Rock Mech.*, Santa Fe, NM, 345–354.
- Rutqvist, J. (1995): A method to determine stress-transmissivity relationship of joints from hydraulic field testing. *Proc., 8th Int. Congress on Rock Mechanics*, Japan, 755–758.
- Sagar, B., Runchal, A. (1982): Permeability of fractured rock: effect of fracture size and data uncertainties. *Water Resour. Res.* 18, 266–274.
- Shimo, M., Iihoshi, S. (1995): Experimental and numerical study on fluid and mass transport through fractured rocks. *Proc., 8th Int. Congress on Rock Mechanics*, Japan, 803–806.
- Snow, D. T. (1969): Anisotropic permeability of fractured media, *Water Resour. Res.* 5, 1273–1289.
- Suri, P., Azeemuddin, M., Zaman, M., Kukreti, A. R., Roegiers, J.-C. (1997): Stress-dependent permeability measurement using the oscillating pulse technique. *J. Petrol. Sci. Eng.* 17, 247–264.
- Takahashi, M., Koide, H., Sugita, Y. (1995): Three principal stress effects on permeability of Shirahama sandstone. *Proc., 8th Int. Congress on Rock Mechanics*, Japan, 729–732.
- Timoshenko, S. (1934): *Theory of elasticity*, 1st edn. McGraw-Hill, New York, 416p.
- Witherspoon, P. A., Wang, J. S. Y., Iwai, K., Gale, J. E. (1980): Validity of Cubic law for fluid flow in a deformable rock fracture. *Water Resour. Res.* 16(6), 1016–1024.
- Zoback, M. D., Byerlee, J. D. (1975): The effect of microcrack dilatancy on the permeability of Westerly granite. *J. Geophys. Res.* 80, 752–755.

**Authors' address:** Dr. Mao Bai, Energy Center P 119, University of Oklahoma, 100 East Boyd, Norman, OK 73019-1014, U.S.A.